ENGINEERING

A magnetically actuated microrobot for targeted neural cell delivery and selective connection of neural networks

Eunhee Kim[1,2], Sungwoong Jeon[1,2], Hyun-Kyu An[3], Mehrnoosh Kianpour[2], Seong-Woon Yu[3], Jin-young Kim[1,2]*†, Jong-Cheol Rah[3,4], Hongsoo Choi[1,2,5]*†

There has been a great deal of interest in the development of technologies for actively manipulating neural networks in vitro, providing natural but simplified environments in a highly reproducible manner in which to study brain function and related diseases. Platforms for these in vitro neural networks require precise and selective neural connections at the target location, with minimal external influences, and measurement of neural activity to determine how neurons communicate. Here, we report a neuron-loaded microrobot for selective connection of neural networks via precise delivery to a gap between two neural clusters by an external magnetic field. In addition, the extracellular action potential was propagated from one cluster to the other through the neurons on the microrobot. The proposed technique shows the potential for use in experiments to understand how neurons communicate in the neural network by actively connecting neural clusters.

INTRODUCTION

Investigating neural connectivity and activity is crucial to understand brain functions such as learning, memory, motion, sensory processing, and decision-making, which are critically dependent on appropriate neural connections (*1*, *2*). In vitro neural networks enable functional analysis, via chemical and electrophysiological methods, to more effectively study the underlying fundamental characteristics of neural network reconstruction and connectivity by providing reproducible analysis before in vivo experiments (*3*, *4*). Controllable and active neural networks in vitro, especially selective connection and active formation of neural networks, may also help the understanding of targeted therapeutics for axonal (re) growth from injured or malfunctioning neurons (*5*, *6*). To engineer the morphology and connectivity of neural cells in vitro, many groups have attempted to form and control cell patterns and directionality of neurite growth in a chemical, physical, or mechanical manner (*7*, *8*). For example, with chemical or physical cell-patterning techniques (*9*), a grid of circular and linear micropatterns was used to geometrically manipulate neural circuits with functional synaptic connections. Yoshida *et al.* (*10*) described a microplate composed of a circle for the neural cell body to adhere to and several protruding straight arms to guide neurite growth. By using the accurate and physical contact of the microbead-attached atomic force microscopy tip to neurites in vitro, new functional neurites have been created and positioned to selectively (re)wire neurites and controllably form neural networks (*11*). However, these complete manual operations could limit the rapid and precise control of neural cells and make it difficult for cells to wirelessly approach tiny or complex sites.

Recently, magnetically actuated microrobots have emerged as promising tools for the accurate delivery of drugs or cells to a target area because of their various advantages, such as precise and wireless three-dimensional (3D) manipulation in physiological environments, accessibility to tiny areas, and use of harmless and low-attenuated energy sources (*12*). In our previous researches, 3D scaffold-type microrobots have been developed, and targeted cell delivery in vitro was carried out using an external magnetic field (*13*–*15*). Recently, magnetically actuated spherical (*15*), helical (*15*–*17*), and burr-like porous spherical microrobots (*18*) have been demonstrated the feasibility of targeted cell delivery in vivo and in vitro. However, these studies were mostly focused on fabricating various microrobot structures and transporting cells loaded on the microrobots under an external power source. To the best of our knowledge, the use of microrobots to mediate neurite alignment and neural connections has not been previously reported. The microgrooved surface topography, which mimics an aligned neurite growth of central nervous system neurons, has been used to facilitate the formation of networks and investigate the effect of neurite alignment in neural tissue engineering (*19*, *20*). Therefore, we used a basic and widely used design of microgrooved surfaces as a proof of concept to achieve neurite alignment and neural network formation. Numerous modeling-based studies have assessed the relationship between neuronal morphology and electrophysiological properties (*21*, *22*). The modulation of the neuronal morphology using microrobots might provide a better understanding of the relationship between neuronal morphology and excitability.

Here, we report a 3D magnetically actuated microrobot capable of guiding the direction of neurite outgrowth and selectively (re) constructing the neural network in vitro. To investigate the neural directionality and functional connectivity, we used primary rat hippocampal cells, which constitute the best-characterized model because of its polarization and widely known stages of network development (*23*, *24*). Using immunofluorescence confocal imaging, the aligned neurite outgrowth and synaptic connections between the neural clusters were observed in the neural network on the microrobot. Moreover, normal physiological functions of the neurons

[1]Department of Robotics Engineering, Daegu Gyeongbuk Institute of Science and Technology (DGIST), Daegu 42988, South Korea. [2]DGIST-ETH Microrobot Research Center, DGIST, Daegu 42988, South Korea. [3]Department of Brain and Cognitive Sciences, DGIST, Daegu 42988, South Korea. [4]Korea Brain Research Institute, Daegu 42988, South Korea. [5]Robotics Research Center, DGIST, Daegu 42988, South Korea.
*Corresponding author. Email: mems@dgist.ac.kr (H.C.), jy.kim@dgist.ac.kr (J.-y.K.)
†These authors contributed equally to this work.

were preserved with a complementary metal-oxide semiconductor–based high-density (HD)–multielectrode array (MEA) system to track the propagation of extracellular axonal signals of the neural clusters connected by the neuron-loaded microrobot (*25*, *26*). The proposed microrobot and its application could act as a fundamental in vitro system capable of the targeted neuronal cell delivery and the formation of an active neural network and, thus, facilitate the study of neural networks and neural connectivity to gain a better understanding of brain function, especially for in vitro study.

RESULTS

Design and fabrication of a microrobot for neural connections

Figure 1A shows the magnetically actuated microrobot that can transport cultured neural cells precisely to link the disconnected neural clusters and form active neural networks, showing reciprocal communication using the HD-MEA system. As illustrated in Fig. 1B, the microrobot has gently sloping ends that were designed for neurites to grow smoothly from the microrobot to the surrounding substrate and vice versa, eventually interconnecting with each other. The top surface of the microrobot also has longitudinal microgrooves (5-μm width by 2-μm depth) that are similar to the width of axons and dendrites (*19*, *20*). These microgrooves were designed to align and direct the outgrowth of neurites toward the sloped ends, where neurites should be newly connected. A rectangular pattern was engraved on the upper left (or lower right) side from the top view as a rollover indicator to recognize that the microrobot was placed in the correct orientation relative to the *z* axis. Otherwise, the gentle sloped ends would become overhang-like ends, which may be too steep for neurites to grow over the surface of the microrobot. Although neurites would manage to outgrow in this case, they could be severely bent and easily broken by even a small external force. Figure 1C shows the fabrication procedure of the microrobot by two-photon polymerization (TPP)–based 3D laser lithography and the deposition of nickel (Ni) and titanium dioxide (TiO_2) layers for magnetic and biocompatible properties, respectively. Figure 1D shows scanning electron microscopy images of the fabricated microrobots with the microgrooves.

Cultivation of neurons and neurite outgrowth on the microrobot

In immunofluorescence images, we visually characterized neurite outgrowth of hippocampal neurons on glass substrates (plain surface) as a control and the microrobots with microgrooves. The number of neurites from neurons increased with time, interconnecting complex neural networks, on both plain and microgrooved surfaces (fig. S1). These immunofluorescence images were then color-mapped by height to observe attachment and cultivation of neurons on a plain surface and the microrobot [Fig. 2, A to F (i)]. We transferred the microrobot onto a glass substrate to be able to visualize the neurite outgrowth after cell loading onto the microrobot [Fig. 2, D to F (i)]. As a result, only a few cells were observed on the glass substrate outside of the microrobot. As the sizes of the neurites (also called axons and dendrites) and the neuronal cell body (also called soma) are generally about ~2 to 5 μm and ~10 to 20 μm thick

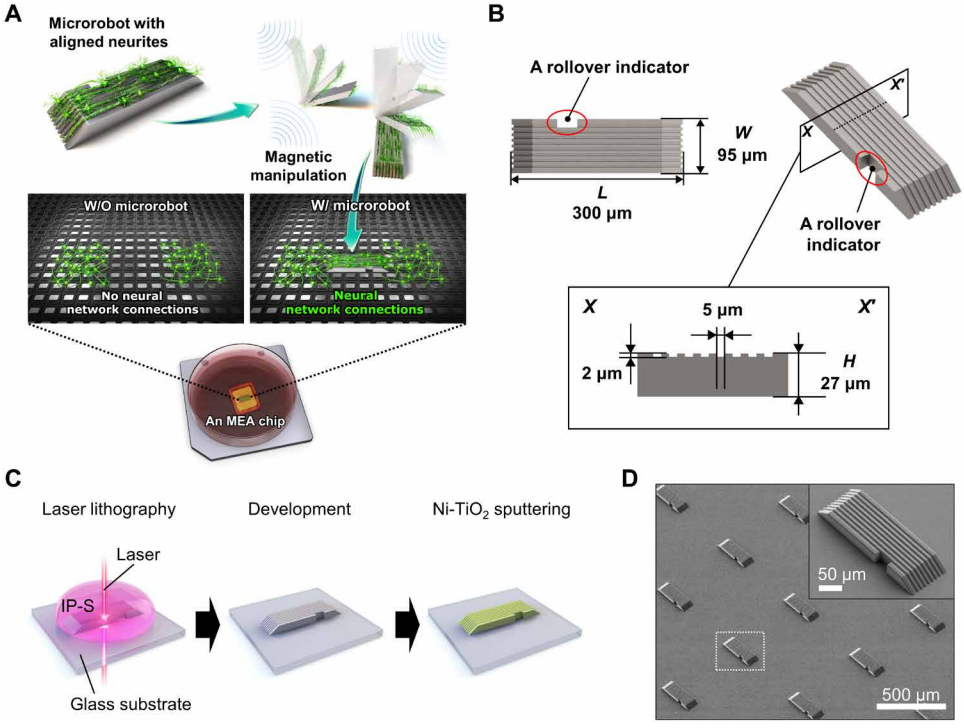

Fig. 1. Schematic illustration and fabrication process of a magnetically actuated microrobot for neural networks. (**A**) Schematic of the active construction between two neural clusters using the microrobot on an HD-MEA chip that can measure axonal signal transmission. (**B**) Computer-aided design images and dimensions of the microrobot. (**C**) Overall fabrication process of the microrobots; two-photon laser lithography and nickel (Ni, for magnetic properties)/titanium oxide (TiO_2, for biocompatibility) deposition. (**D**) Scanning electron microscopy images of the fabricated microrobot with the microgrooves.

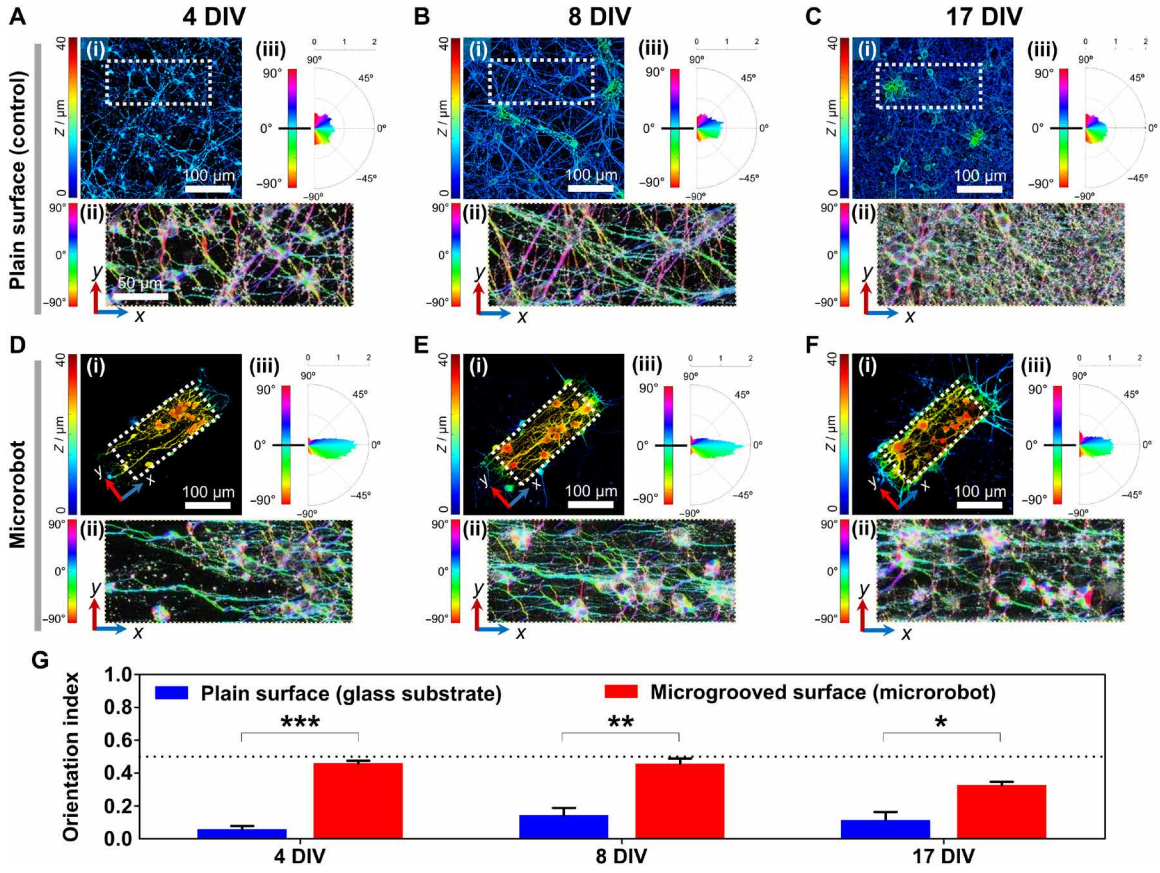

Fig. 2. Effects of the microgrooves on the microrobot for hippocampal cell alignment. (**A** to **C**) Height coding fluorescence confocal micrographs of β-III tubulin (TUBB3)– and 4′,6-diamidino-2-phenylindole (DAPI)–stained hippocampal neurons and orientation histogram of neurites on glass substrates as a control after (A) 4 days in vitro (DIV), (B) 8 DIV, and (C) 17 DIV from plating (0 DIV). (**D** to **F**) Height coding fluorescence confocal micrographs of neurons on the microrobots with microgrooves after (D) 4 DIV, (E) 8 DIV, and (F) 17 DIV from plating (0 DIV). Subimages indicate (i) micrographs color-mapped by height relative to *z*-axis scale, (ii) color-mapped micrographs by orientation angles of the neurites of the white dotted area in each (i) image, and (iii) polar frequency histograms of orientation angles of the neurites in each (ii) image. (**G**) Plot of OI calculated from orientation angles of neurites on a plain surface and the microgrooved surface (microrobot) at 4, 8, and 17 DIV.

(*27*), respectively, the neurons cultured on a plain surface formed neural networks within the corresponding height range of the cells. By contrast, the height of the cells on the microrobot was increased up to approximately 40 μm when cultured on the microrobot because of the height of the microrobot (27 μm). These results demonstrated that neurons were successfully cultured on the microrobot and extended their neurites with no notable effects on viability compared to the control.

From the immunofluorescence micrographs of the neurites, we also analyzed local orientation distribution of neurites on a plain surface [Fig. 2, A to C (ii and iii)] and on the longitudinal microgrooves of the microrobot [Fig. 2, D to F (ii and iii)] to characterize the effects of the surface pattern on the directionality of neurite growth (the longitudinal direction in fig. S2A). The longitudinal microgrooves played a crucial role in directing the growth of neurites [Fig. 2, A to F (ii and iii)]. The neurites cultured on a plain surface grew out from the neurons in random directions for 17 days and showed a polychromatic and dull histogram, indicating no directional specificity [Fig. 2, A to C (ii and iii)]. However, neurites tended to align along the microgrooves during cultivation on the microrobot [Fig. 2, D to F (ii)], indicating higher directional specificity to 0° than neurons on the plain surface in the polar histogram [Fig. 2, D to F (iii)].

The orientation indices (OIs) were calculated to quantify the directional specificity of neurites. OI values of 1 indicate completely parallel relative to the longitudinal direction (aligned in fig. S2B) of the microgrooves on the microrobot, and OI values closer to 0 represent isotropic directionality. As shown in Fig. 2G, OI values of neurites cultured on the microgrooves were approximately four times higher than those of neurites cultured on the plain surface, with values of 0.46, 0.46, and 0.33 versus 0.06, 0.15, and 0.12 at 4, 8, and 17 days in vitro (DIV), respectively. To assess the effect of surrounding cells on the alignment, we prepared a cuboid structure of the same size as the microrobot but without microgrooves. As shown in fig. S3, the alignment of neurites on the cuboid at 8 DIV had an OI of 0.19, which was not significantly different from that of the plain surface (glass substrate) at the same day (OI = 0.15; Fig. 2G). This finding suggests that the directionality of neurites was still random and that there was no difference in tendency in the presence (plain surface) or absence (cuboid) of surrounding cells. Therefore, the use of the alignment results [Fig. 2, A to C (i)] on the plain surface instead of the cuboid was appropriate. In addition, the sloped ends of the microrobot mainly led to smooth extension and connection of neurites between the microrobot and surrounding surfaces [Fig. 2, D to F (i)]. On the sloped ends, neurites may not

only overgrow from the microrobot toward the surrounding surface but may also be newly connected in random directions, forming a complex neural network, rather than aligning along the microgrooves. Therefore, the lower directionality of neurites was measured on the sloped ends (OI = −0.13 and −0.15 at left and right sloped ends, respectively) in comparison to the other areas on the microgrooves, especially at 17 DIV (OI = 0.41) (fig. S4). However, it was still higher than that of the plain surface (OI = 0.04) without any guiding structure to direct outgrowth of neurites. Although OI values on the plain surface were analyzed within the confined area at different angles (45° and 90°), they did not have specific directionality, showing values of only up to 0.18 at 8 DIV on 0° images (fig. S5). On the basis of the OI values, no specific directionality of the neurites was found on the plain surface. In contrast, the longitudinal microgrooves resulted in alignment of the neurites up to four times greater than on the plain surface. These results indicated that the developed microrobot has potential for transporting and culturing neurons over 2 weeks as well as directing and connecting neurite outgrowth in the desired orientation. It may be useful to study brain functionality in the mimicked structure in vitro, as the brain has directionally aligned axonal tracts to perform neural functions.

Manipulation of the microrobot on an array of neural clusters

As it is important to precisely deliver and locate neurons cultured on the microrobot onto the desired position, for active connection of neural networks, the magnetic actuation of the microrobot was characterized in vitro. As shown in Fig. 3A, the microrobot was manipulated on an array of neural clusters (ANC) by magnetic fields generated by a linear superposition of individual fields from the eight electromagnetic coil system in a hemispherical configuration and observed by a charge-coupled device (CCD) camera on top. An array of 500 μm by 500 μm neural clusters with a gap of about 200 μm was patterned on a glass substrate, as explained in fig. S6. To determine how accurately the developed microrobot can be controlled using a magnetic field, we measured the positioning errors in x and y directions and the angular error. As shown in fig. S7, we used a grid with a distance of 1 mm. We controlled the microrobot toward the orthogonal point at the top right where the two yellow dashed lines (horizontal and vertical) meet. The number of microrobots used for this experiment was four. The mean positional errors were ~7% in the x axis and ~14% in the y axis, where the length and width of the microrobot were 300 and 95 μm, respectively (fig. S7). The mean angular error in aligning the microrobot between neural clusters was 1.9°. With this level of controllability in position and orientation, the developed microrobot can be precisely placed between neural clusters with a gap of 200 μm using the appropriate magnetic fields. The microrobot used here has an anisotropic shape, and it can be aligned in the longitudinal direction between two neural clusters depending on the magnetic field applied. The rotating magnetic field allows the microrobot to propel by tumbling (*28*). However, the extra weight added by the cells attached to the microrobot might affect the microrobot's rotational motion. Despite this extra weight, the position and orientation of the microrobot can be precisely controlled in response to the rotating magnetic field. The microrobot with neurons was quickly moved close to the target by a rotating magnetic field with a magnetic field intensity of 20 mT at 1.2 Hz. Then, the orientation of the microrobot was slowly changed under a constant magnetic field (20 mT) to position on the desired gap

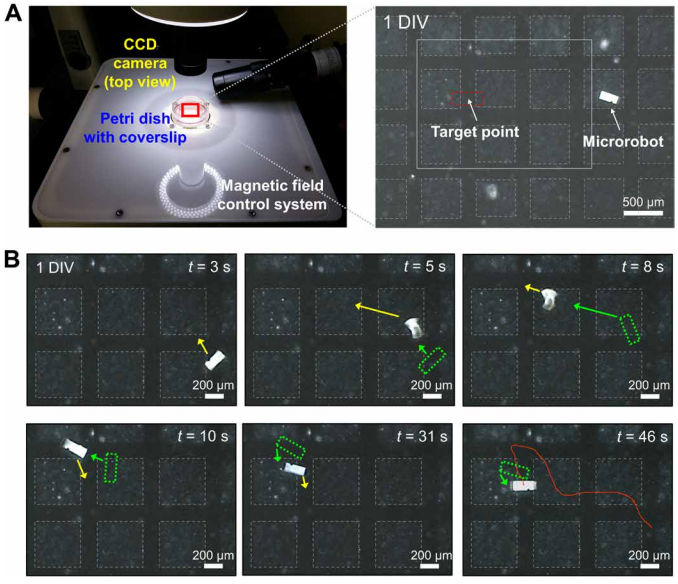

Fig. 3. Magnetic manipulation of the microrobot on a glass substrate with an array of neural clusters. (**A**) Experimental setup for microrobot manipulation using the magnetic field control system (left) and a glass substrate (right) with an array of neural clusters (ANC) cultured for 1 DIV. White dashed boxes indicate neural networks. The red dashed box indicates the target point of the microrobot. (**B**) Snapshots of positional control of the microrobot between two neural clusters during magnetic manipulation in the area presented in (A) (white solid-line box, right). Green dotted boxes indicate the position of the microrobot in the previous snapshot.

between the neural clusters, where the neural network is to be formed in vitro (Fig. 3B and movie S1). As a result, the neurons attached to the microrobot reached the target position within 10 s and precisely aligned to connect the desired neural clusters in 1 min. The cell viability of cells cultured on a cell culture dish (2D culture) was assessed before and after the magnetic manipulation of the microrobot for 10 min. As shown in fig. S8, there was no notable difference before and after the manipulation, suggesting that the motion of the microrobot did not affect cell viability.

Morphology-based characterization of neural connections using the microrobot

To assess the feasibility of neural connections using the microrobot, we investigated the morphology of neurons after the successful positioning of the neuron-loaded microrobot between the desired neural clusters on the ANC. Figure 4 shows the neurite outgrowth and neural connections on the glass substrate with and without the microrobot at 17 DIV. As the microrobot was deposited with thin opaque metal layers of Ni and TiO_2, the neurite outgrowth on the microrobot appeared to be disturbed in the bright-field images. Therefore, immunofluorescence imaging was performed using a confocal upright microscope to observe neurite outgrowth on the microrobot. Figure 4A shows the ANC without the microrobot as a control. Neurite outgrowth and neural connections were observed in the cluster (Fig. 4a′), but there were no neurites or neural connections in the gap between the two neural clusters (Fig. 4a′′). For height coding images (Fig. 4B), neural clusters were shown to be formed within a height of up to about 20 μm, which is the typical height of neurons. While neurons generated and extended neurites

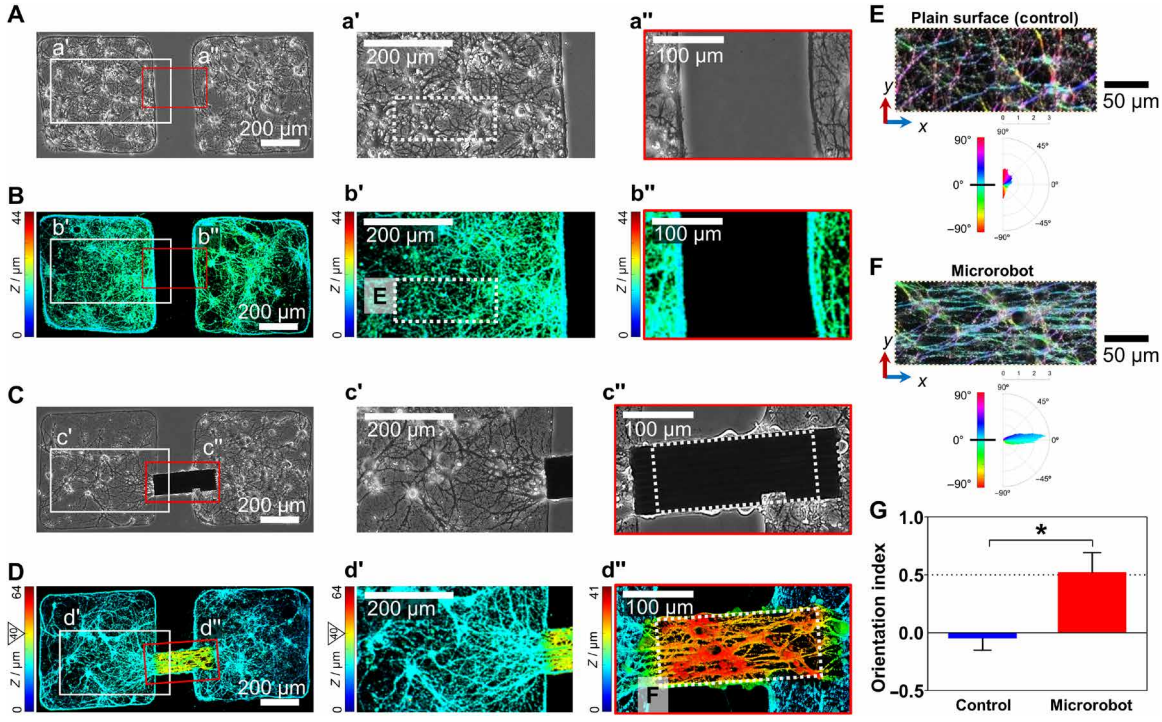

Fig. 4. Hippocampal neural connections between neural clusters with and without the microrobot at 17 DIV. (**A** and **B**) Morphology [bright-field images in (A) and height coding fluorescence confocal micrographs in (B)] of hippocampal neurons of two neural clusters without the microrobot as a control. (**C** and **D**) Morphology [bright-field images in (C) and height coding fluorescence confocal micrographs in (D)] of hippocampal neurons of two neural clusters with the microrobot where cells were seeded. White dotted boxes presented in the left panels indicate the areas of a′, b′, c′, and d′, respectively. Red solid-line boxes presented in the left panels indicate the areas of a′′, b′′, c′′, and d′′, respectively. (**E**) Color-mapped micrograph (top) and polar frequency histogram (bottom) by orientation angles of the neurites of the white dotted area in a′ and b′ as a control. (**F**) Color-mapped micrograph (top) and polar frequency histogram (bottom) by orientation angles of the neurites of the white dotted area in c′′ and d′′ on the microrobot. (**G**) Plot of OI calculated from orientation angles of neurites on the control and on the microrobot. Cultures were immunostained for neurites in green (TUBB3) and stained for nuclei in blue (DAPI).

inside the cluster (Fig. 4b′), no neurite outgrowth was observed in the gap of the neural clusters (Fig. 4b′′), similar to the result in the bright-field images.

In contrast, the two separate neural clusters were morphologically connected through the microrobot, where the microrobot was placed by magnetic manipulation between the clusters at 1 DIV and cultured for 17 days (Fig. 4C). Bright-field images at 4, 8, 14, and 17 DIV showed neurite outgrowth in the area around the microrobot over time (fig. S9). In particular, a remarkable change in outgrowth of neurites was observed in the neural clusters on both sides of the microrobot. The image on 17 DIV showed greater neurite outgrowth compared to other images (Fig. 4, c′ and c′′; see also fig. S9). Height coding images showed that neurons were distributed in the range of about 40 μm because of the microrobot height of 27 μm (Fig. 4D). Figure 4d′ shows that the neurites inside the neural cluster interconnected with neurites on the microrobot, and Fig. 4d′′ also shows that the neurite outgrowth aligned toward the left and right neural clusters on the ANC. In comparison, neurite outgrowth in controls showed a random neurite distribution, while cells on the microrobot showed aligned neurite extension (Fig. 4, E and F). Neurites on the microrobot extended mainly along the microgrooves with an OI of 0.52, while neurites on the glass substrate without the microrobot showed random growth with an OI of −0.05 (Fig. 4G). We also found that neurites between the two separate neural clusters were successfully reconstructed, with the morphological connections established using the microrobot and magnetic manipulation. Furthermore, the microrobot itself and manipulation of the microrobot did not interfere with neurite outgrowth or the morphological neural network, as observed by neurite extensions on the ANC with and without the microrobot.

Electrophysiological characterization of neural connectivity through the microrobot

To investigate the electrophysiological interconnection of the neural clusters by the microrobot, we recorded electrophysiological signals from the neurons using the HD-MEA system. Figure 5A shows the magnetic manipulation of the microrobot on the ANC in the HD-MEA chip at 1 DIV (movie S2). Figure 5B shows the spontaneous spike amplitude map (SSAM) of neural activities of the ANC with the microrobot (yellow dashed box) (see also fig. S10). Neural activity recorded from the HD-MEA chip coincided with the morphology photograph of the ANC observed (Fig. 5C). Therefore, we could successfully monitor the overall viability and activity of the neural cultures during cultivation, as well as identify the interconnected neural networks by the microrobot without the need for microscopic investigation.

To identify and track the neural network signals, we analyzed the axonal action potential (AP) propagation between the two neural clusters with and without the neuron-loaded microrobot at 17 DIV (Fig. 6). We can detect propagating APs because the largest AP

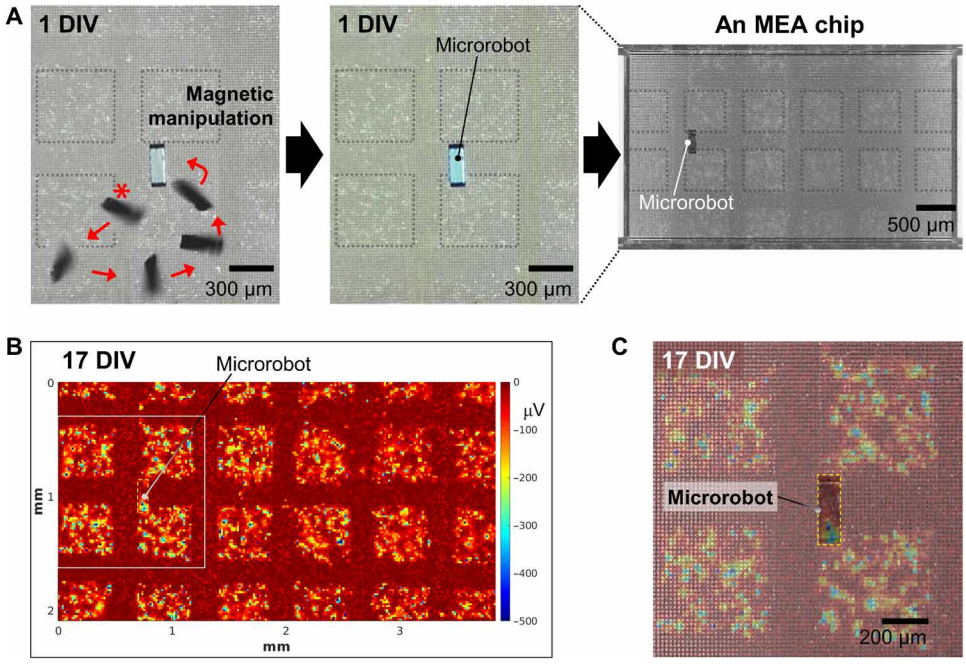

Fig. 5. Magnetic manipulation of the microrobot and the spontaneous activity map on an HD-MEA chip with an ANC. (**A**) Photograph of the moving microrobot (left) during magnetic manipulation. Red arrows represent the trajectory of the moving microrobot. The red asterisk indicates the starting point. The microrobot with cells was placed (middle) between separate neural networks after magnetic manipulation at 1 DIV. A photograph of the HD-MEA chip (right) taken at 2 DIV (1 day after the microrobot placement) is shown. Dotted lines indicate an ANC. (**B**) Spontaneous activity map of the hippocampal neural culture with the microrobot on an HD-MEA chip with an ANC at 17 DIV. Amplitudes recorded by each electrode were averaged and color-coded. (**C**) Overlap image of the spontaneous activity map at 17 DIV of the white boxed area in (B) and a photograph of the HD-MEA chip of the right panel in (A). Yellow dashed boxes indicate the position of the microrobot in (B) and (C).

signals typically occur in the regions proximal to the soma and travel through the activated axonal parts on the electrodes (*21*). In the neural clusters without the microrobot, AP propagation mostly traveled in the bottom neural cluster (zone 1), and neural signals hardly crossed to the upper neural cluster (zone 2) (Fig. 6A and movie S3). As shown in Fig. 6B, the average peak-to-peak amplitudes of the triggered APs were 40, 24, and 45 μV at the electrodes labeled 1 to 3, respectively, in the bottom neural cluster (zone 1). However, no APs were detected at the electrodes labeled 4 to 6 in the upper neural cluster (zone 2). Therefore, these results indicated that the neural clusters without the microrobot were not physically and functionally connected by neurons. In contrast, the presence of the microrobot between the two neural clusters enabled axonal signal propagation from the bottom neural cluster (zone 3) to the upper neural cluster (zone 4) (Fig. 6C and movie S4). Spike- and/or stimulation-triggered averaging of the neural signals enabled identification of neural activities (*22*). The average amplitudes of the triggered APs were 116, 172, 100, 41, 105, and 145 μV peak to peak at the electrodes labeled 1 to 6, respectively (Fig. 6D). These results indicated that the microrobot with the neurons can form physical and functional neural connections and can also induce AP propagation. The availability of the multiple electrodes around an axon enables averaging in space. Moreover, averaging in the time domain revealed the spatial arrangements of the axonal segments through their electrical footprints by averaging 40 to 60 AP waveforms (*25*, *29*). Thus, electrodes that captured the electrical signal with the largest amplitude in each separate cluster were adopted and analyzed in this study.

To ensure reliable neural responses from the neural clusters of interest, we stimulated different positions in the neural clusters with and without the microrobot while recording APs. We could not detect any axonal signal propagation when the electrodes in the spot without neurons were stimulated (movie S5). These results suggested that there would also be no functional connections between the disconnected neural networks. Neural signals propagated simultaneously into both zone 3 and zone 4 when the electrical stimulation was evoked at the single electrode that was in the middle of the microrobot (Fig. 6, E and F, and movie S6). We can predict that axonal projections were extended at the bottom of the microrobot because it would not be possible to stimulate axons on the top surface of the microrobot using the electrode. Together, we found that our microrobot contributed functionally and morphologically to form and connect neural networks.

DISCUSSION

Here, we showed that it is possible to morphologically and functionally connect separate neural clusters for in vitro targeted neural connections using a magnetically actuated microrobot. Our microrobot has the advantage of reproducible, selective, and precise connectivity. We have previously reported on the fabrication and magnetic manipulation of various microrobots and obtained similar results on the morphology and placement of the microrobot. We have also optimized various parameters for the formation of neural clusters (i.e., cell patterns on the glass substrate and the MEA chip) and neural connections using the microrobot. After optimization,

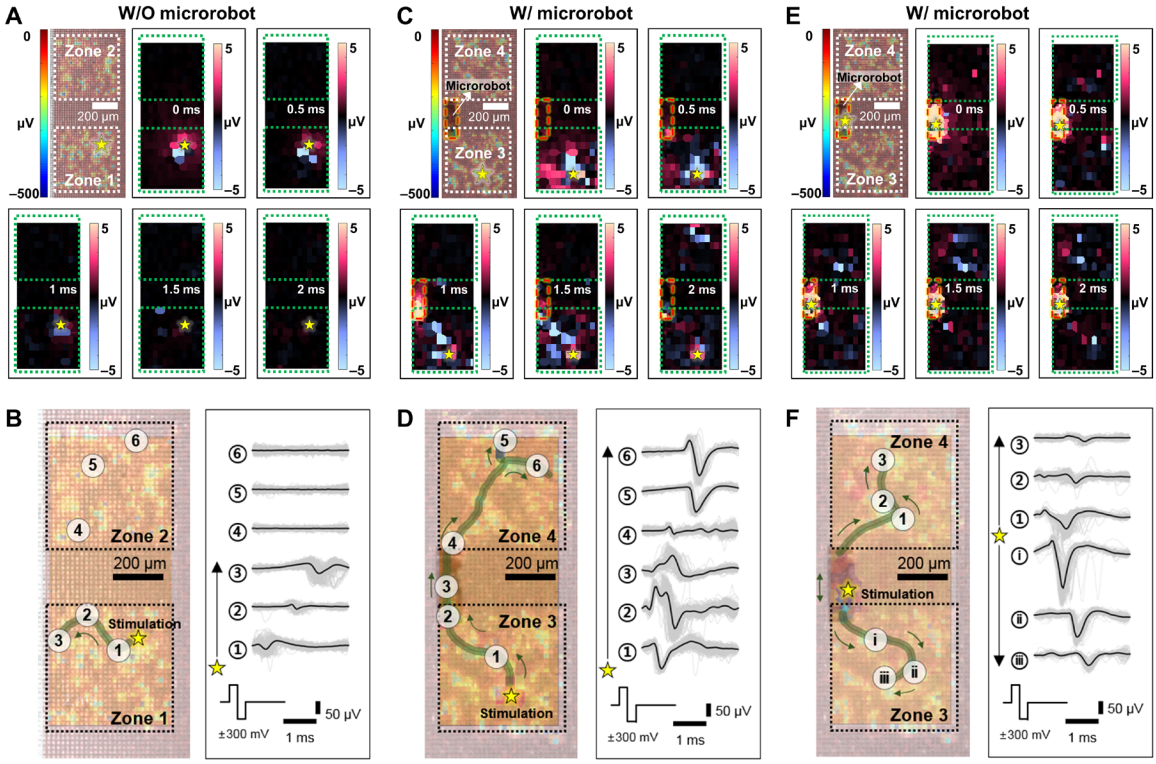

Fig. 6. Electrical stimulation and AP propagation of hippocampal neurons cultured without the microrobot and with the microrobot on an ANC at 17 DIV. (**A** and **B**) Evoked neural activity by stimulation of (A) an ANC without the microrobot and (B) AP propagation in 1 to 3 (left) and AP waveforms (right) from electrodes corresponding to the left panel. (**C** and **D**) Evoked neural activity by stimulation of (C) an ANC with the microrobot and (D) AP propagation in 1 to 6 (left) and AP waveforms (right) from electrodes corresponding to the left panel. (**E** and **F**) Evoked neural activity by stimulation between neural clusters with the microrobot in (E) and both directions of AP propagation of 1 to 3 and i to iii (left) and AP waveforms (right) from electrodes corresponding to the left panel in (F). Yellow stars indicate stimulation electrodes in all figures. Red dashed boxes indicate the microrobot location in (C) and (E). Gray lines and black lines represent single trials and the median overall trials, respectively, in the right panels of (B), (D), and (F).

we managed to bridge individual neural clusters while maintaining neural network morphology and cell viability (Fig. 4). As microrobots reported previously have shown cell compatibility using human embryonic kidney 293 cells (*13*), olfactory receptor neurons (*14*), HCT116 cells, hippocampal neural stem cells, and human nasal inferior turbinate–derived mesenchymal stem cells (*15*), this microrobot using the same fabrication method could also be successfully applied to primary neurons. To provide enhanced biocompatibility of the microrobot for cell-based analysis applications, the material for magnetic actuation can be replaced with Fe_3O_4 nanoparticles that have stable cytocompatibility compared to that of Ni (*30*, *31*). In contrast to techniques that require the use of a micromanipulator or a micropipette, methods using our proposed microrobot and magnetic control system can be carried out while maintaining the in vitro cell culture environment. After the microrobot is submerged into the medium, it can be wirelessly controlled by an external magnetic field so that cells and medium are not exposed to the outside air.

The same fabrication and manipulation techniques proposed in this study may also be applicable to single-cell microrobot structures to form individual neurite connections using an external magnetic field. The use of microrobots allows neuroengineers to design neuronal circuits in vitro more reliably and safely by connecting individual neurites, as reported in previous studies (*10*, *32*). Hence, the development of single-cell level microrobots will enable the formation and connection of single neurites or cells. The magnetic field control system, which is one of the robotic systems, would be essential for the precise micromanipulation by the microrobot used in this study and other cell-sized microrobots to form a single neural connection or artificial neural networks. We have previously developed magnetic microrobots with sizes ranging from tens to hundreds of micrometers, allowing for precise and safe manipulations. Future studies are required to assess the ability of next-generation microrobots with various sizes to deliver neurons or connect single and multiple neurites that are difficult to access by hand. Future studies are required to establish the optimal shape of the cylindrical tube to enable stable and durable alignment of neurites and improve the formation and control of neural networks (*33*–*35*).

While pyramidal neurons in the hippocampus and the neocortex have a clear polarity in vivo, cultured neurons are often mixed with various cell types and tend to have random directionality. The lack of polarity is problematic since the columnar orientation and connectivity in the neocortex have been proposed as providing basic computational modules in the neocortices (*36*). The manipulation of the axonal outgrowth and neuronal directionality will enable us to precisely construct neural and synaptic networks that more closely resemble the in vivo conditions (e.g., CA3-CA1 or thalamocortical layer IV circuits). Distal dendrites of hippocampal cornu

ammonis 1 (CA1) neurons receive inputs, mainly from the entorhinal cortex, whereas proximal dendrites are innervated by hippocampal CA3 neurons (*37*). Although random connectivity (i.e., CA1-to-CA1) will account for most of the synapses in the conventional cultures of hippocampal neurons, we could cultivate CA1 neurons with proximal CA3 inputs and distal entorhinal synapses with the currently developed microrobot.

A number of limitations can affect neural activity signals, which are detected from neurons cultured on the HD-MEA chip. First, numerous neurons that overlapped each other may prevent the analysis of the recorded signals. As depicted in our data (Fig. 6, C and E, and movies S4 and S6), because of the abundance of cells used to create neural clusters, the neural activity may appear as if no propagating APs exist or AP propagation velocity is reduced because cells can be simultaneously activated (*38*). Therefore, shortening the duration of the cell culture or reducing the cell density might improve the measurement of AP signals. Second, during AP propagation, stimulation sites and voltage magnitudes may be applied individually depending on each cell, as the stimulation could affect intrinsic neuronal plasticity (*39*). By contrast, as we applied the same electrical voltage of 300 mV to cells, spike traces of evoked neurons on the HD-MEA chip would all have been different (Fig. 6, B, D, and F). Third, the electrode quality and impedance can vary with regard to the extent of sufficient stimulus magnitudes or response to cells (*25*). Despite these limitations in electrophysiological data, in this study, a single consistent pathway between zone 3 and zone 4 was observed in the results for each stimulation (Fig. 6, C and D, and movie S4). Therefore, our approach could open the possibility for analysis based on electrophysiological stimulation and recording with diverse microrobots and different cells.

We expect our results to be a potential starting platform for advanced controllable in vitro models of artificial neural networks. For example, neural activity could be assessed using various microrobots with different microgroove designs according to the extent of alignment in connected compartmental neural networks. Moreover, the development of microrobots with improved controllability may enable us to reconstruct more sophisticated artificial neural networks. We are currently in the process of establishing complex and diverse connections using various microrobots for future research. The use of the developed microrobot will also facilitate investigation of the electrophysiological properties of specific synaptic connections and verify the effect of drugs on specific synapses with high sensitivity. In particular, numerical changes or changes in strength in corticostriatal synaptic connections and impaired plasticity have been reported in patients with Parkinson's disease and obsessive-compulsive disorder (*40*–*42*). Therefore, mimicking the corticostriatal synaptic connection in cultured neurons using microrobots could provide a powerful platform for the development and testing of therapeutic interventions and improve our understanding of neural networks.

MATERIALS AND METHODS

Design and fabrication of the microrobot

The microrobot was designed in SolidWorks (Dassault Systèmes SolidWorks Corp., Waltham, MA), a computer-aided design program used for 3D design. The design parameters of the microrobot were determined on the basis of the sizes of the neurons and neurites. Figure 1B shows the 3D design of the microrobot used in this study.

To fabricate the microrobot, TPP microfabrication was conducted with a 3D laser lithography system (Nanoscribe Photonic Professional GT; Nanoscribe GmbH, Eggenstein-Leopoldshafen, Germany), referred to as Nanoscribe (*43*, *44*). In Nanoscribe, a 100-fs pulsed 780-nm laser was focused via a 25× NA (numerical aperture) 0.8 objective lens (Carl Zeiss, Jena, Germany) directly into the IP-S photoresist (Nanoscribe GmbH). The exposed resist by the laser was polymerized, and 3D microrobots were fabricated by this writing process (Fig. 1C). The microrobot was designed with a length of 300 μm, which was a distance capable of stably reaching and forming neurites in 2 days. After TPP, the nonpolymerized monomer solution was removed by immersing the substrate in the SU-8 developer (MicroChem Corp., Newton, MA) for 20 min. The substrate was then rinsed in isopropyl alcohol (JT Baker, Phillipsburg, NJ) and dried under a stream of dry nitrogen gas. For determination of the magnetic properties and biocompatibility of the microrobot, 170-nm Ni and 200-nm TiO_2 thin films were deposited on the fabricated 3D structure using a sputter coater (SRN-110; Sorona Inc., Pyeongtaek, South Korea).

Isolation and culture of the primary hippocampal neurons

Animal experiments were conducted in accordance with the regulations of the Animal Experiment Ethics Committee of the Daegu Gyeongbuk Institute of Science and Technology (DGIST) (approval no. DGIST-IACUC-19050903-08). Pregnant Sprague-Dawley rats (15 weeks of age, female, 200 g) were purchased from KOATECH (Gyunggi-do, South Korea). For anesthesia and euthanasia, the pregnant Sprague-Dawley rats were exposed to inhalation of CO_2 gas. Primary hippocampal neurons were prepared from the hippocampi of embryonic day 18 rats. The hippocampi were trypsinized and dissociated with 0.25% trypsin-EDTA (Thermo Fisher Scientific, Waltham, MA; catalog no. 25200056) for 2 min and mechanically triturated. The cell suspension was washed with phosphate-buffered saline (PBS; Thermo Fisher Scientific; catalog no. 10010023) with 1% penicillin and streptomycin (Thermo Fisher Scientific; catalog no. 15140122) and filtrated using a cell strainer with 40-μm pores. The hippocampal cell cultures were maintained in supplemented Neurobasal medium (Thermo Fisher Scientific; catalog no. 21103049) with the addition of 1% L-glutamine (Thermo Fisher Scientific; catalog no. 25030149), 2% B-27 supplement (Thermo Fisher Scientific; catalog no. 17504044), and 1% penicillin/streptomycin. Primary neural cells were seeded and cultured on the microrobot in a humidified incubator (5% CO_2 and 37°C) for 17 days to characterize the cultivation of neurons and the biocompatibility of the microrobot. The neurons were also cultured on a typical glass substrate coated using a previously established method as a control and compared to the neurons on the microrobot to investigate outgrowth of neurites directed by the longitudinal microgrooves on the microrobot.

Immunofluorescence staining

Primary hippocampal neurons on glass substrates and microrobots at 4, 8, and 17 DIV were immunostained to visualize the neural cell marker β-III tubulin (TUBB3) in green and the nuclei with 4′,6-diamidino-2-phenylindole (DAPI) in blue. First, cells were fixed with 4% paraformaldehyde (Sigma-Aldrich, St. Louis, MO) in PBS for 30 min at room temperature, followed by washing three times with PBS. They were then permeabilized in 0.25% Triton X-100 (Sigma-Aldrich) for 1 hour at room temperature, followed by washing three times with PBS. Next, cells were incubated in blocking

buffer consisting of PBS supplemented with 1% bovine serum albumin (Sigma-Aldrich) for 1 hour at room temperature. Primary antibody to β-III tubulin (Abcam, Cambridge, UK; catalog no. ab18207) was diluted to 1:1000 (v/v) in blocking buffer and incubated with the neuronal cultures at 4°C overnight, followed by washing three times in PBS for 15 min each time. For secondary antibody staining, Alexa Fluor 488 (Thermo Fisher Scientific; catalog no. A11008) was diluted 1:1000 (v/v) and incubated in blocking buffer for 2 hours at room temperature and then washed three times in PBS for 15 min each time. Samples were counterstained with DAPI (1:1000 dilution; Thermo Fisher Scientific; catalog no. D1306) to visualize the nuclei.

Confocal laser scanning microscopy

Fluorescence images were acquired using a confocal laser scanning microscope (LSM 780; Carl Zeiss) equipped with solid-state lasers (405, 488, 555, and 639 nm). ZEN software (Carl Zeiss) was used for image postprocessing, such as maximum intensity projection and 3D reconstruction, to carefully observe and analyze the morphology of the neurites in 2D and 3D microenvironments. The immunofluorescently stained cells on a glass substrate were subjected to high-resolution imaging in PBS with a 40× water immersion objective lens to prevent desiccation of samples during imaging. To assess the alignment of neurites, *z*-stacked images (range, 40 μm; interval, 1.38 μm) in two channels (green for β-III tubulin and blue for DAPI) were acquired simultaneously with a 40× NA 1.15 water immersion objective to create maximum intensity projection images. These images were color-mapped by height (*z* axis) using a transparency rendering mode and depth coding [Fig. 2, A to F (i)]. The ANC without the microrobot (Fig. 4B) was imaged with a 10× objective in a *z*-stack mode (range, 44 μm; interval, 4 μm) to reconstruct single composite images. In the case of the ANC with the microrobot where neurons were loaded (Fig. 4D), the investigation was performed with a 10× objective in the *z*-stack mode (range, 64 μm; interval, 4 μm) and 40× objective in the *z*-stack mode (range, 41 μm; interval, 1 μm) to reconstruct 3D images.

Measurement of neural orientations

After primary neural cells were attached and cultured on a flat substrate and the microgrooved microrobot, neural orientations of the neurons were measured and compared to investigate the effects of the microgrooves on neurite outgrowth. When neurons were cultured on the microrobot, the microgrooves on the microrobot faced upward (Fig. 1B); otherwise, the slope ends would be placed upside down, making it easier to form neural connections among the neurites on the glass substrate and the microrobot. As indicated with a white dotted box in Fig. 2 [A to F (i)], the neurons to be analyzed were confined to a square area of 228 μm × 95 μm (length × width) on the surfaces, which is the same area as the top surface of the microrobot, except for the sloped ends on both sides. Neurons in the confined area were color-mapped by orientation angles of neurons as shown in Fig. 2 [A to F (ii)]. Their polar histograms were then produced for graphical presentation of the directional specificity of the neurites, as shown in Fig. 2 [A to F (iii)]. For example, as more neurites aligned in a specific angle, the histogram became less polychromatic, narrower, and longer along the specific angle. The OrientationJ plugin of ImageJ software (National Institutes of Health, Bethesda, MD; https://imagej.nih.gov/ij/) was used to quantitatively analyze the directionality of neurites from the confocal fluorescence images (*45*). OrientationJ computed local orientations of each pixel in the confocal images, which were encoded in colors (color-mapped by orientation angles of neurons) and displayed directly on the images [Fig. 2, A to F (ii)]. Maximum intensity projection images from *z*-stacked images were used to analyze the orientation of β-III tubulin–labeled cells and neurites on a glass substrate (plain surface) and the microgrooves of the microrobot (Fig. 2, A to F, and fig. S1). Both color-mapped images and local orientations ranging from −90° to 90° were acquired by OrientationJ. The OI can denote the extent of alignment of neurites to the longitudinal direction (the *x* axis) of the microgrooves (fig. S2). Therefore, to quantify the directional specificity of neurites, OI was calculated with the frequency data of local orientations, giving the following (*46*)

$$\mathrm{OI}\,(\theta_i) = \frac{\sum_{\theta=-90^\circ}^{90^\circ} \cos(2(\theta - \theta_i))\, N(\theta)}{\sum_{\theta=-90^\circ}^{90^\circ} N(\theta)} \quad (1)$$

where θ_i is the alignment angle of interest, θ is the local orientation angle, and $N(\theta)$ is the number of pixels (frequency) at a given local orientation angle. We defined the *x* direction as 0° (fig. S2) and evaluated orientation of alignments relative to the *x* direction (i.e., $\theta_i = 0$). Therefore, OI can be rewritten as

$$\mathrm{OI} = \frac{\sum_{\theta=-90^\circ}^{90^\circ} \cos(2\theta)\, N(\theta)}{\sum_{\theta=-90^\circ}^{90^\circ} N(\theta)} \quad (2)$$

The OI values of 1 and −1 indicate completely parallel and orthogonal alignments, respectively, relative to the *x* axis, which is the longitudinal direction of the microgrooves on the microrobot, and the OI values closer to 0 represent isotropic directionality. Polar frequency histograms of neurites or cells were generated by plotting normalized frequencies (i.e., $N(\theta)/\sum_{\theta=-90^\circ}^{90^\circ} N(\theta)$) from the angular range (OriginPro; OriginLab Corp., Northampton, MA). The angular color scale was identical to the color coding of the OrientationJ. The upper limit of the radial direction in all polar frequency histograms was fixed at 2% for better visibility [Fig. 2, A to F (iii)].

ANC preparation using polydimethylsiloxane stencil

The ANC was prepared and cultured on a glass substrate and an HD-MEA chip using polydimethylsiloxane (PDMS) stencil (fig. S6). The PDMS stencil was prepared using an SU-8 master mold and was cut to 5 mm by 5 mm and placed on the glass substrate and the HD-MEA chip. For cell attachment, polyethyleneimine and laminin were coated on the surfaces that were not covered with the PDMS stencil (*25*). The ANC was obtained by removing the PDMS stencil at 24 hours after seeding cells and cultured for 17 days. A single neural cluster was about 500 μm by 500 μm, and the gap between the neural clusters was about 200 μm. More information is presented in the Supplementary Materials.

Microrobot manipulation

An electromagnetic coil system (Mini-Mag; Aeon Scientific AG, Schlieren, Switzerland) was used to control the position and orientation of the proposed microrobot. The Mini-Mag is composed of a combination of eight electromagnetic coils for five degrees of freedom (DOF; 3-DOF position, 2-DOF pointing orientation) (*47*). A maximum magnetic field of 20 mT and a magnetic field gradient of 2 T m^{-1} can be generated from the eight electromagnetic coils with ferromagnetic cores. By rotating the magnetic field, the microrobot was controlled to a target area by rolling motion in the first step.

Then, the orientation of the microrobot was accurately changed to connect the two neural clusters in the second step. The magnetic field strength for driving the microrobot was 20 mT, and the rotating magnetic field frequency was between 0 and 1.2 Hz. The manipulation of the microrobot on the glass substrate and the HD-MEA chip was recorded using a VZM 600i zoom imaging lens (Edmund Optics Inc., Barrington, NJ) linked with a CCD camera (Grasshopper; Point Grey Research Inc., Richmond, BC, Canada) (movies S1 and S2).

HD-MEA recording and stimulation protocols

All analyses described below were performed using MATLAB R2018b (MathWorks Inc., Natick, MA) with "Signal Processing" and "Statistics and Machine Learning" toolboxes. During the cultivation period, extracellular activity using the HD-MEA system (MaxOne; MaxWell Biosystems AG, Basel, Switzerland) was monitored and recorded inside the incubator. All extracellular data were digitally band-pass–filtered (500 to 3000 Hz) before recording.

Spontaneous spike amplitude map

Spontaneous firing activity was typically observed after 1 week in culture. The entire array to cover all 26,400 electrodes was scanned for spontaneous activity. Signal recording was performed sequentially from dense blocks of 27 electrode configurations for 20 s per configuration. Spikes were detected at every electrode by a threshold level of 4.5× signal SDs, and the negative peak amplitudes for all the electrodes were displayed in SSAMs (shown in Fig. 5B and fig. S10) using color coding. The SSAMs visualized the viability of the cultures and the positions of spontaneously active neurons on the array.

Electrodes at local peaks in the SSAM

Electrodes with large spike amplitudes indicated that active neurons were located nearby and, therefore, indicated suitable sites for recording and stimulation. The respective recording and stimulation sites needed to be identified automatically on the basis of the SSAM because some experiments were required to record neural signals from many neurons or to stimulate many neurons. Therefore, we used sites representing local peaks in the SSAM. First, all the electrodes with negative peak amplitudes exceeding a predefined threshold were selected. In a second step, if multiple neighboring electrodes had exceeded the threshold, then only the electrodes closest to the local peak amplitude were further considered. The threshold value was set manually, while a MATLAB function provided the information on how many selected electrodes resulted in a particular value. Depending on the specific experiment, the threshold value was varied to yield the desired number of electrodes.

Hippocampal neurons on the array typically yielded a single local peak coinciding with the location of the electrode yielding the largest signal amplitude. For aggregations of neurons, in contrast, the footprints of the cells primarily overlapped. Therefore, the resulting number of local peaks in regions of neuron aggregation was significantly smaller than the number of cells. Avoiding the selection of many electrodes underneath aggregations of multiple neurons was particularly crucial for the stimulation experiments. Because of these large numbers of neurons, multiple electrodes may simultaneously stimulate the same cell.

Stimulation-triggered recordings

To identify and track the neural network signals, individual neurons in the neural cluster areas with and without the microrobot were activated using balanced positive-first biphasic voltage pulses because of their effectiveness in electrical stimulation (*48*). Voltage pulses had phase durations of 200 μs and amplitudes of ±300 mV. Three hundred stimuli were applied at a frequency of 3 Hz with a sampling rate of 20 kHz to one electrode, indicated by a yellow star in Fig. 6, in all stimulation protocols. An electrode was connected to a stimulation channel. To detect stimulus-triggered responses of neurons in separate neural clusters of interest, we designed a custom configuration with 843 electrodes underlying detectable neural compartments (fig. S10C). The triggered AP waveforms (300 trials), designated as a stimulation-triggered footprint, were acquired by scanning this configuration. Recorded stimulus-triggered responses were temporally aligned according to the downswing of the biphasic stimulation. Aligned responses were used to reconstruct the footprints (Fig. 6) and make AP propagation movies (movies S3 to S6). AP propagation evoked by the electrical stimulation was visualized between the two neural clusters for 2 ms.

Statistical analysis

Statistical significance was determined from independent experiments in triplicate. All statistical analyses were performed with GraphPad Prism (GraphPad Software, San Diego, CA) using the parametric unpaired *t* test with Welch's correction (Fig. 2G). Error bars indicate SD from three samples. $^{*}P < 0.05$, $^{**}P < 0.01$, and $^{***}P < 0.001$. Calculated *P* values are also specified.

SUPPLEMENTARY MATERIALS

Supplementary material for this article is available at http://advances.sciencemag.org/cgi/content/full/6/39/eabb5696/DC1

REFERENCES AND NOTES

1. J. Y. Hua, S. J. Smith, Neural activity and the dynamics of central nervous system development. *Nat. Neurosci.* **7**, 327–332 (2004).
2. A. J. Silva, Y. Zhou, T. Rogerson, J. Shobe, J. Balaji, Molecular and cellular approaches to memory allocation in neural circuits. *Science* **326**, 391–395 (2009).
3. S. Marom, G. Shahaf, Development, learning and memory in large random networks of cortical neurons: Lessons beyond anatomy. *Q. Rev. Biophys.* **35**, 63–87 (2002).
4. P.-M. Lau, G.-Q. Bi, Synaptic mechanisms of persistent reverberatory activity in neuronal networks. *Proc. Natl. Acad. Sci. U.S.A.* **102**, 10333–10338 (2005).
5. F. Bradke, J. W. Fawcett, M. E. Spira, Assembly of a new growth cone after axotomy: The precursor to axon regeneration. *Nat. Rev. Neurosci.* **13**, 183–193 (2012).
6. A. J. Aguayo, G. M. Bray, M. Rasminsky, T. Zwimpfer, D. Carter, M. Vidal-Sanz, Synaptic connections made by axons regenerating in the central nervous system of adult mammals. *J. Exp. Biol.* **153**, 199–224 (1990).
7. A. C. Greene, C. M. Washburn, G. D. Bachand, C. D. James, Combined chemical and topographical guidance cues for directing cytoarchitectural polarization in primary neurons. *Biomaterials* **32**, 8860–8869 (2011).
8. S. Roth, G. Bugnicourt, M. Bisbal, S. Gory-Fauré, J. Brocard, C. Villard, Neuronal architectures with axo-dendritic polarity above silicon nanowires. *Small* **8**, 671–675 (2012).
9. K. Hennig, I. Wang, P. Moreau, L. Valon, S. DeBeco, M. Coppey, Y. A. Miroshnikova, C. Albiges-Rizo, C. Favard, R. Voituriez, M. Balland, Stick-slip dynamics of cell adhesion triggers spontaneous symmetry breaking and directional migration of mesenchymal cells on one-dimensional lines. *Sci. Adv.* **6**, eaau5670 (2020).
10. S. Yoshida, T. Teshima, K. Kuribayashi-Shigetomi, S. Takeuchi, Mobile microplates for morphological control and assembly of individual neural cells. *Adv. Healthc. Mater.* **5**, 415–420 (2016).
11. M. H. Magdesian, G. M. Lopez-Ayon, M. Mori, D. Boudreau, A. Goulet-Hanssens, R. Sanz, Y. Miyahara, C. J. Barrett, A. E. Fournier, Y. De Koninck, P. Grütter, Rapid mechanically controlled rewiring of neuronal circuits. *J. Neurosci.* **36**, 979–987 (2016).
12. S. Schuerle, A. P. Soleimany, T. Yeh, G. M. Anand, M. Häberli, H. E. Fleming, N. Mirkhani, F. Qiu, S. Hauert, X. Wang, B. J. Nelson, S. N. Bhatia, Synthetic and living micropropellers for convection-enhanced nanoparticle transport. *Sci. Adv.* **5**, eaav4803 (2019).
13. S. Kim, F. Qiu, S. Kim, A. Ghanbari, C. Moon, L. Zhang, B. J. Nelson, H. Choi, Fabrication and characterization of magnetic microrobots for three-dimensional cell culture and targeted transportation. *Adv. Mater.* **25**, 5863–5868 (2013).
14. S. Lee, S. Kim, S. Kim, J.-Y. Kim, C. Moon, B. J. Nelson, H. Choi, A capsule-type microrobot with pick-and-drop motion for targeted drug and cell delivery. *Adv. Healthc. Mater.* **7**, 1700985 (2018).

15. S. Jeon, S. Kim, S. Ha, S. Lee, E. Kim, S. Y. Kim, S. H. Park, J. H. Jeon, S. W. Kim, C. Moon, B. J. Nelson, J.-y. Kim, S.-W. Yu, H. Choi, Magnetically actuated microrobots as a platform for stem cell transplantation. *Sci. Robot.* **4**, eaav4317 (2019).
16. Z. Wu, J. Troll, H.-H. Jeong, Q. Wei, M. Stang, F. Ziemssen, Z. Wang, M. Dong, S. Schnichels, T. Qiu, P. Fischer, A swarm of slippery micropropellers penetrates the vitreous body of the eye. *Sci. Adv.* **4**, eaat4388 (2018).
17. H.-W. Huang, F. E. Uslu, P. Katsamba, E. Lauga, M. S. Sakar, B. J. Nelson, Adaptive locomotion of artificial microswimmers. *Sci. Adv.* **5**, eaau1532 (2019).
18. J. Li, X. Li, T. Luo, R. Wang, C. Liu, S. Chen, D. Li, J. Yue, S.-h. Cheng, D. Sun, Development of a magnetic microrobot for carrying and delivering targeted cells. *Sci. Robot.* **3**, eaat8829 (2018).
19. L. Cai, L. Zhang, J. Dong, S. Wang, Photocured biodegradable polymer substrates of varying stiffness and microgroove dimensions for promoting nerve cell guidance and differentiation. *Langmuir* **28**, 12557–12568 (2012).
20. M. Kamudzandu, Y. Yang, P. Roach, R. A. Fricker, Efficient alignment of primary CNS neurites using structurally engineered surfaces and biochemical cues. *RSC Adv.* **5**, 22053–22059 (2015).
21. C. D. Aizenman, E. J. Huang, D. J. Linden, Morphological correlates of intrinsic electrical excitability in neurons of the deep cerebellar nuclei. *J. Neurophysiol.* **89**, 1738–1747 (2003).
22. Z. F. Mainen, T. J. Sejnowski, Influence of dendritic structure on firing pattern in model neocortical neurons. *Nature* **382**, 363–366 (1996).
23. H. J. Ahn, C. M. Hernandez, J. M. Levenson, F. D. Lubin, H.-C. Liou, J. D. Sweatt, c-Rel, an NF-κB family transcription factor, is required for hippocampal long-term synaptic plasticity and memory formation. *Learn. Mem.* **15**, 539–549 (2008).
24. K. Goslin, G. Banker, Experimental observations on the development of polarity by hippocampal neurons in culture. *J. Cell Biol.* **108**, 1507–1516 (1989).
25. D. J. Bakkum, U. Frey, M. Radivojevic, T. L. Russell, J. Müller, M. Fiscella, H. Takahashi, A. Hierlemann, Tracking axonal action potential propagation on a high-density microelectrode array across hundreds of sites. *Nat. Commun.* **4**, 2181 (2013).
26. M. Radivojevic, D. Jäckel, M. Altermatt, J. Müller, V. Viswam, A. Hierlemann, D. J. Bakkum, Electrical identification and selective microstimulation of neuronal compartments based on features of extracellular action potentials. *Sci. Rep.* **6**, 31332 (2016).
27. J. Park, S. Kim, S. I. Park, Y. Choe, J. Li, A. Han, A microchip for quantitative analysis of CNS axon growth under localized biomolecular treatments. *J. Neurosci. Methods* **221**, 166–174 (2014).
28. K. E. Peyer, L. Zhang, B. J. Nelson, Bio-inspired magnetic swimming microrobots for biomedical applications. *Nanoscale* **5**, 1259–1272 (2013).
29. U. Frey, U. Egert, F. Heer, S. Hafizovic, A. Hierlemann, Microelectronic system for high-resolution mapping of extracellular electric fields applied to brain slices. *Biosens. Bioelectron.* **24**, 2191–2198 (2009).
30. J.-y. Kim, S. Jeon, J. Lee, S. Lee, J. Lee, B. O. Jeon, J. E. Jang, H. Choi, A simple and rapid fabrication method for biodegradable drug-encapsulating microrobots using laser micromachining, and characterization thereof. *Sens. Actuators B* **266**, 276–287 (2018).
31. J. Park, C. Jin, S. Lee, J.-Y. Kim, H. Choi, Magnetically actuated degradable microrobots for actively controlled drug release and hyperthermia therapy. *Adv. Healthc. Mater.* **8**, 1900213 (2019).
32. S. Yoshida, M. Kato-Negishi, S. Takeuchi, Assembly and connection of micropatterned single neurons for neuronal network formation. *Micromachines* **9**, 235 (2018).
33. K. S. Katiyar, L. A. Struzyna, J. P. Morand, J. C. Burrell, B. Clements, F. A. Laimo, K. D. Browne, J. Kohn, Z. Ali, H. C. Ledebur, D. H. Smith, D. K. Cullen, Tissue engineered axon tracts serve as living scaffolds to accelerate axonal regeneration and functional recovery following peripheral nerve injury in rats. *Front. Bioeng. Biotechnol.* **8**, 492 (2020).
34. T. F. Teshima, H. Nakashima, Y. Ueno, S. Sasaki, C. S. Henderson, S. Tsukada, Cell assembly in self-foldable multi-layered soft micro-rolls. *Sci. Rep.* **7**, 17376 (2017).
35. P. Froeter, Y. Huang, O. V. Cangellaris, W. Huang, E. W. Dent, M. U. Gillette, J. C. Williams, X. Li, Toward intelligent synthetic neural circuits: Directing and accelerating neuron cell growth by self-rolled-up silicon nitride microtube array. *ACS Nano* **8**, 11108–11117 (2014).
36. V. B. Mountcastle, The columnar organization of the neocortex. *Brain* **120**, 701–722 (1997).
37. P. Andersen, R. Morris, D. Amaral, T. Bliss, J. O'Keefe, *The Hippocampus Book* (Oxford Univ. Press, 2007).
38. T. Dugladze, D. Schmitz, M. A. Whittington, I. Vida, T. Gloveli, Segregation of axonal and somatic activity during fast network oscillations. *Science* **336**, 1458–1461 (2012).
39. M. S. Grubb, J. Burrone, Activity-dependent relocation of the axon initial segment fine-tunes neuronal excitability. *Nature* **465**, 1070–1074 (2010).
40. R. M. Villalba, A. Mathai, Y. Smith, Morphological changes of glutamatergic synapses in animal models of Parkinson's disease. *Front. Neuroanat.* **9**, 117 (2015).
41. C. R. Gerfen, D. J. Surmeier, Modulation of striatal projection systems by dopamine. *Annu. Rev. Neurosci.* **34**, 441–466 (2011).
42. G. Akopian, J. P. Walsh, Pre- and postsynaptic contributions to age-related alterations in corticostriatal synaptic plasticity. *Synapse* **60**, 223–238 (2006).
43. T. Bückmann, N. Stenger, M. Kadic, J. Kaschke, A. Frölich, T. Kennerknecht, C. Eberl, M. Thiel, M. Wegener, Tailored 3D mechanical metamaterials made by dip-in direct-laser-writing optical lithography. *Adv. Mater.* **24**, 2710–2714 (2012).
44. F. Klein, B. Richter, T. Striebel, C. M. Franz, G. von Freymann, M. Wegener, M. Bastmeyer, Two-component polymer scaffolds for controlled three-dimensional cell culture. *Adv. Mater.* **23**, 1341–1345 (2011).
45. R. Rezakhaniha, A. Agianniotis, J. T. C. Schrauwen, A. Griffa, D. Sage, C. V. C. Bouten, F. N. van de Vosse, M. Unser, N. Stergiopulos, Experimental investigation of collagen waviness and orientation in the arterial adventitia using confocal laser scanning microscopy. *Biomech. Model. Mechanobiol.* **11**, 461–473 (2012).
46. S. H. Kim, S.-K. Im, S.-J. Oh, S. Jeong, E.-S. Yoon, C. J. Lee, N. Choi, E.-M. Hur, Anisotropically organized three-dimensional culture platform for reconstruction of a hippocampal neural network. *Nat. Commun.* **8**, 14346 (2017).
47. S. Schuerle, S. Erni, M. Flink, B. E. Kratochvil, B. J. Nelson, Three-dimensional magnetic manipulation of micro- and nanostructures for applications in life sciences. *IEEE Trans. Magn.* **49**, 321–330 (2013).
48. D. A. Wagenaar, J. Pine, S. M. Potter, Effective parameters for stimulation of dissociated cultures using multi-electrode arrays. *J. Neurosci. Methods* **138**, 27–37 (2004).
49. J. H. Choi, H. Lee, H. K. Jin, J.-s. Bae, G. M. Kim, Micropatterning of neural stem cells and Purkinje neurons using a polydimethylsiloxane (PDMS) stencil. *Lab Chip* **12**, 5045–5050 (2012).
50. U. V. Nägerl, N. Eberhorn, S. B. Cambridge, T. Bonhoeffer, Bidirectional activity-dependent morphological plasticity in hippocampal neurons. *Neuron* **44**, 759–767 (2004).

Acknowledgments: We are grateful to all the members of DGIST-ETH Microrobot Research Center and Bio-Microrobotics Lab for sincere help and comment. We also thank the CCRF of the DGIST and MaxWell Biosystems AG for helpful discussions and technical supports. **Funding:** This work was supported by the Global Research Laboratory, the Bio & Medical Technology Development Program, and the Brain Research Program of the National Research Foundation of Korea (NRF) funded by the Ministry of Science and ICT (no. 2017K1A1A2013237, no. 2017M3A9G8084463, and no. 2018M3C7A1056275) and the DGIST R&D Program funded by the Ministry of Science and ICT (20-CoE-BT-02). **Author contributions:** E.K. and S.J. designed, fabricated, and manipulated the microrobots and wrote the manuscript. E.K., S.J., H.-K.A., and M.K. performed the isolation of primary hippocampal neurons from rat embryos. E.K. cultured the hippocampal neurons, performed electrophysiological experiments, and analyzed the data. S.-W.Y. guided analysis of the hippocampal neuron–related data. J.-y.K. guided microrobot experiments using the HD-MEA system, analyzed the data, and wrote the manuscript. J.-C.R. analyzed neural network and electrophysiological data and reviewed the manuscript. H.C. designed the study, led the project, and wrote the manuscript. All authors read, edited, and accepted the manuscript. **Competing interests:** The authors declare that they have no competing interests. **Data and materials availability:** All data needed to evaluate the conclusions in the paper are present in the paper and/or the Supplementary Materials. Additional data related to this paper may be requested from the authors.

Submitted 4 March 2020
Accepted 10 August 2020
Published 25 September 2020
10.1126/sciadv.abb5696

Citation: E. Kim, S. Jeon, H.-K. An, M. Kianpour, S.-W. Yu, J.-y. Kim, J.-C. Rah, H. Choi, A magnetically actuated microrobot for targeted neural cell delivery and selective connection of neural networks. *Sci. Adv.* **6**, eabb5696 (2020).